

# Seismic inversion using hybrid quantum neural networks

Divakar Vashisth\*<sup>1</sup>, Rohan Sharma<sup>2</sup>, Tapan Mukerji<sup>1</sup> and Mrinal K. Sen<sup>3</sup>

<sup>1</sup>Department of Energy Science and Engineering, Stanford University, USA, <sup>2</sup>Department of Applied Geophysics, Indian Institute of Technology (Indian School of Mines) Dhanbad, India, <sup>3</sup>Institute for Geophysics, The University of Texas at Austin, USA

email: \*divakar.vashisth98@gmail.com

## Abstract

Quantum computing leverages qubits, exploiting superposition and entanglement to solve problems intractable for classical computers, offering significant computational advantages. Quantum machine learning (QML), which integrates quantum computing with machine learning, holds immense potential across various fields but remains largely unexplored in geosciences. However, its progress is hindered by the limitations of current NISQ hardware. To address these challenges, hybrid quantum neural networks (HQNNs) have emerged, combining quantum layers within classical neural networks to leverage the strengths of both paradigms. To the best of our knowledge, this study presents the first application of QML to subsurface imaging through the development of hybrid quantum physics-informed neural networks (HQ-PINNs) for seismic inversion. We apply the HQ-PINN framework to invert pre-stack and post-stack seismic datasets, estimating P- and S-impedances. The proposed HQ-PINN architecture follows an encoder-decoder structure, where the encoder (HQNN), processes seismic data to estimate elastic parameters, while the decoder utilizes these parameters to generate the corresponding seismic data based on geophysical relationships. The HQ-PINN model is trained by minimizing the misfit between the input and predicted seismic data generated by the decoder. We systematically evaluate various quantum layer configurations, differentiation methods, and quantum device simulators on the inversion performance, and demonstrate real-world applicability through the individual and simultaneous inversion cases of the Sleipner dataset. The HQ-PINN framework consistently and efficiently estimated accurate subsurface impedances across the synthetic and field case studies, establishing the feasibility of leveraging QML for seismic inversion, thereby paving the way for broader applications of quantum computing in geosciences.

## Introduction

The concept of quantum computing originated in the 1980s and has since evolved into one of the most pioneering and dynamic fields in computational science. Richard Feynman's seminal 1982 lecture "*Simulating Physics with Computers*", often considered the foundation of quantum computing, introduced the idea of using quantum systems to simulate complex quantum phenomena, recognizing the exponential cost of simulating such systems with classical computers (Feynman, 1982; Preskill, 2023). This concept was further advanced by David Deutsch, who raised the critical question of whether quantum computers could outperform classical systems in solving problems beyond quantum physics. He subsequently formalized the principles of universal quantum computation, laying the groundwork for practical exploration (Deutsch, 1985). The 1990s witnessed pivotal theoretical breakthroughs in quantum computing. Bernstein and Vazirani's algorithm (Bernstein and Vazirani, 1993) demonstrated the advantages of quantum algorithms in structured problems, while Simon's algorithm (Simon, 1994) provided the first formal evidence of an exponential quantum speedup. These discoveries, along with advances in quantum Fourier transforms, directly influenced Peter Shor's algorithm for integer factorization (Shor, 1994), which demonstrated that quantum computers could efficiently solve problems central to modern cryptography, capturing global scientific interest and propelling quantum computing into mainstream discourse.

In the modern era, quantum computing signifies a paradigm shift in addressing computational challenges, particularly those beyond the reach of classical methods. At its core lies the quantum bit, or qubit, which leverages fundamental quantum properties like superposition and entanglement to encode and process information in ways fundamentally distinct from classical bits (Nielsen and Chuang, 2010). While classical bits exist in one of two definite states, 0 or 1, qubits exist in a superposition of both states until measured, allowing quantum algorithms to explore multiple computational paths simultaneously through quantum interference. This enables certain types of parallel computations that have no classical counterpart. Additionally, quantum entanglement- a phenomenon where qubits exhibit strong correlations regardless of spatial separation- facilitates coordinated operations between qubits, enhancing computational efficiency. While entanglement does not enable faster-than-light communication, it plays a crucial role in quantum information processing, quantum teleportation, and error correction schemes necessary for scalable quantum computation. Together, these principles position quantum computers as potential game-changers, capable of outperforming classical systems in specialized problem domains. Researchers have increasingly sought to leverage these capabilities for diverse applications, including solving linear systems of equations (Harrow et al., 2009; Bravo-Prieto et al., 2023; Wang et al., 2024b), optimization problems (Perdomo-Ortiz et al., 2012; Farhi et al., 2014; Peruzzo et al., 2014; Neukart et al., 2017), and machine learning (Schuld et al., 2015).

Quantum Machine Learning (QML) represents a rapidly emerging synergy between quantum computing and traditional machine learning, aiming to augment the latter by leveraging the computational advantages of quantum systems. The implementation of QML varies based on whether its key components- data representation and computational processing- are realized using classical or quantum methodologies (Alchieri et al., 2021). However, the current era of Noisy Intermediate-Scale Quantum (NISQ) devices introduces significant hardware limitations, such as qubit decoherence, gate errors, and restricted scalability, which constrain the feasibility of fully quantum implementations for large-scale machine learning tasks (Preskill, 2018). To address these challenges, hybrid quantum-classical frameworks have emerged as a practical alternative. These frameworks integrate quantum and classical processors, leveraging their respective strengths. By offloading specific computational tasks to classical systems and reserving quantum processors for areas where they offer a distinct advantage, hybrid algorithms mitigate the limitations of NISQ devices. This approach enables the development of practical and scalable solutions to tackle complex computational challenges in the near term.

Notable advancements in QML include Quantum Support Vector Machines (Rebentrost et al., 2014), Quantum Neural Networks (Farhi and Neven, 2018), Quantum K-Nearest-Neighbour algorithm (Dang et al., 2018), Quantum Evolutionary Neural Networks (Henderson et al., 2020), the Q-means algorithm (Kerenidis et al., 2019), and Quantum Principal Component analysis (Lloyd et al., 2014). Notably, a significant focus of these algorithms has been on classification and clustering tasks. Beyond these foundational developments, QML has demonstrated considerable potential across multiple disciplines, including molecular chemistry (Sajjan et al., 2022), financial modeling (Orús et al., 2019), high-energy physics (Guan et al., 2021), and medical imaging (Landman et al., 2022).

The interdisciplinary impact of quantum computing continues to expand as it addresses computationally intensive challenges across diverse fields. Geophysics, with its reliance on high-dimensional data and complex computational tasks, has emerged as a promising yet relatively underexplored frontier for quantum computing and QML. There have been a few exploratory contributions to this field. Schade et al. (2024), demonstrated that 1D elastic wave equation could be solved exponentially faster using quantum computing compared to classical methods under certain conditions. Wright et al. (2024) presented quantum circuits tailored for simulating 1D acoustic wave equation on NISQ devices. Additionally, quantum annealing- a specialized quantum computing paradigm designed for optimization- has also shown promise in geophysical applications. Dukalski et al. (2023) employed quantum annealers to estimate refraction residual statics for seismic data processing. Vashisth and Lessard (2024) and Vashisth et al. (2025) utilized quantum annealers to predict subsurface impedances from seismic data, showcasing the first application of quantum computing for seismic inversion. Further, Zaidenberg et al. (2021) and Sebastianelli et al. (2021, 2023) explored hybrid QML frameworks for image classification tasks in earth observation and remote sensing.

These advancements underscore the potential of quantum computing to address computational challenges in geosciences. Our study contributes to this ongoing effort by introducing the Hybrid Quantum Physics-Informed Neural Network (HQ-PINN), a novel framework that integrates quantum computing with physics-informed neural networks for the inversion of seismic data. The adoption of a physics-informed approach is motivated by the efficacy of physics-informed neural networks (PINNs) compared to traditional supervised learning frameworks in geophysical inversion. Unlike supervised learning, which relies heavily on large labelled datasets (well log data) for training, PINNs embed physical relationships into the training process eliminating the need for large labelled datasets (Biswas et al. 2019; Dhara and Sen, 2022; Vashisth and Mukerji, 2022; Liu et al., 2023; Sharma et al., 2024). This ensures that the predictions are both geologically and physically consistent. Moreover, fully supervised training of quantum neural networks requires repeated quantum circuit evaluations for large datasets. This could introduce substantial computational overhead, which may undermine the quantum advantage. To address these challenges, our work combines the strengths of quantum computing and PINNs, offering a promising approach for large-scale geophysical inversion tasks.

This paper begins with an overview of the theoretical foundations of quantum computing and its integration with machine learning. We then provide a detailed description of the proposed HQ-PINN framework for seismic inversion. The efficacy of HQ-PINNs is demonstrated through applications to synthetic seismic datasets, including both post-stack and pre-stack data. We also assess the performance of HQ-PINNs in estimating subsurface impedances from seismic data by varying quantum layer configurations, differentiation methods, and quantum device simulators. The HQ-PINN framework is then applied to the Sleipner dataset, showcasing its capability to handle real-world seismic data. Finally, we discuss the broader implications of leveraging HQ-PINNs for geophysical inversion and its potential to address overarching challenges in the field of geosciences.

## **Quantum Computing and Quantum Machine Learning**

In this section, we provide a brief overview of the theoretical foundations of quantum computing and quantum machine learning. For a more comprehensive discussion, we refer readers to Nielsen and Chuang (2010) and Schuld and Petruccione (2021). Qubits are the fundamental units of information in quantum computing, analogous to bits in classical computing. However, unlike classical bits, which can only exist in one of two definite states (0 or 1), qubits can exist in a superposition of these states. This superposition is mathematically represented in Dirac notation (or bra-ket notation) as:

$$|\psi\rangle = \alpha|0\rangle + \beta|1\rangle, \quad (1)$$

where  $|\psi\rangle$  is a vector in a Hilbert space, and  $|0\rangle$  and  $|1\rangle$  are the basis vectors, represented in matrix form as:

$$|0\rangle = \begin{bmatrix} 1 \\ 0 \end{bmatrix}, |1\rangle = \begin{bmatrix} 0 \\ 1 \end{bmatrix}. \quad (2)$$

The coefficients  $\alpha$  and  $\beta$  are complex numbers that determine the probability of measuring the qubit in a particular state, with the normalization condition:  $|\alpha|^2 + |\beta|^2 = 1$  ensuring that the total probability sums to 1. According to the Born rule, when a qubit is measured, its state collapses to one of the basis states,  $|0\rangle$  or  $|1\rangle$ , with probabilities  $|\alpha|^2$  and  $|\beta|^2$  respectively. This collapse is an irreversible process due to quantum measurement. To perform desired computations, the state of a qubit must be manipulated and this is achieved using quantum gates.

Quantum gates are operations (unitary transformations) that manipulate qubits by altering their probability amplitudes and relative phases. These gates are mathematically represented by unitary matrices, meaning they preserve the norm of the qubit's state vector, ensuring that quantum operations are reversible. Mathematically, a unitary matrix  $U$  satisfies the condition  $U^\dagger U = U U^\dagger = I$  where  $U^\dagger$  is the conjugate transpose (Hermitian adjoint) of  $U$ , and  $I$  is the identity matrix. A sequence of quantum gates applied to a set of qubits constitutes a quantum circuit, which serves as the computational backbone of quantum algorithms.

Single-qubit gates can be visualized as rotations on the Bloch sphere (*Figure 1*), a geometrical representation where the state of a qubit is depicted as a point on a unit sphere in three-dimensional space. The qubit's state can be parametrized using spherical coordinates  $\theta$  and  $\phi$ , expressed as:

$$|\psi\rangle = \cos(\theta/2)|0\rangle + e^{i\phi}\sin(\theta/2)|1\rangle. \quad (3)$$

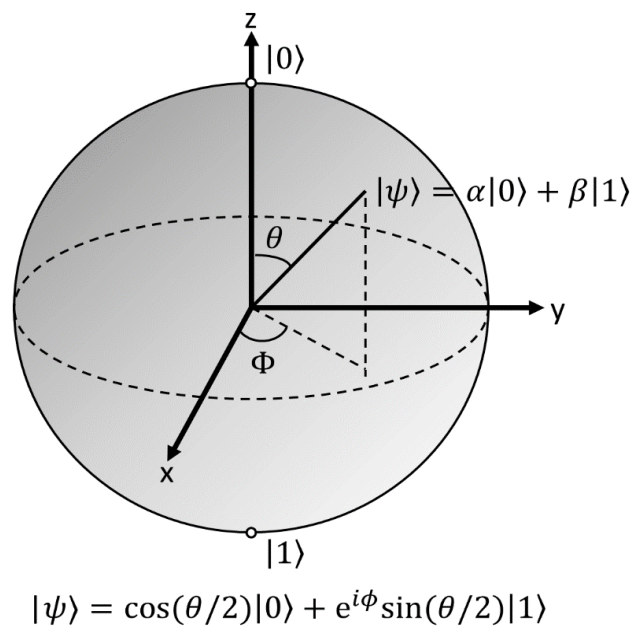


**Figure 1** The Bloch sphere illustrating the quantum state of a single qubit  $|\psi\rangle$  in the Hilbert space. Quantum gate operations manipulate  $|\psi\rangle$  by performing unitary transformations, which correspond to rotations of the state vector around the Bloch sphere.

Here,  $\theta$  (polar angle) determines the relative weight (probability distribution) of  $|0\rangle$  and  $|1\rangle$ , while  $\phi$  (azimuthal angle) introduces a relative phase between the basis states. This representation emphasizes the qubit's complex probabilistic nature and its evolution through quantum gates. Quantum gates correspond to rotations of the state vector  $|\psi\rangle$  on the Bloch sphere, allowing precise control over qubit states. A general single-qubit rotation gate  $R(\theta, \phi, \lambda)$  is defined as:

$$R(\theta, \phi, \lambda) = \begin{bmatrix} \cos \frac{\theta}{2} & -e^{i\lambda} \sin \frac{\theta}{2} \\ e^{i\phi} \sin \frac{\theta}{2} & e^{i(\phi+\lambda)} \cos \frac{\theta}{2} \end{bmatrix}. \quad (4)$$

This general rotation gate enables flexible transformations of qubit states, forming the basis for more complex quantum operations. Some commonly used quantum gates include:

**1) The Rotation gates  $\{R_X(\theta), R_Y(\theta), R_Z(\theta)\}$ :** The rotation gates  $R_X(\theta)$ ,  $R_Y(\theta)$ , and  $R_Z(\theta)$ , perform rotations of a qubit state around the  $X$ ,  $Y$  and  $Z$  axes of the Bloch sphere by an angle  $\theta$ , respectively. They are fundamental in quantum computing for precise qubit state manipulation and are mathematically represented as:

$$R_X(\theta) = \begin{bmatrix} \cos\left(\frac{\theta}{2}\right) & -i \sin\left(\frac{\theta}{2}\right) \\ -i \sin\left(\frac{\theta}{2}\right) & \cos\left(\frac{\theta}{2}\right) \end{bmatrix}, \quad (5a)$$

$$R_Y(\theta) = \begin{bmatrix} \cos\left(\frac{\theta}{2}\right) & -\sin\left(\frac{\theta}{2}\right) \\ \sin\left(\frac{\theta}{2}\right) & \cos\left(\frac{\theta}{2}\right) \end{bmatrix}, \quad (5b)$$

$$R_Z(\theta) = \begin{bmatrix} e^{-i\frac{\theta}{2}} & 0 \\ 0 & e^{i\frac{\theta}{2}} \end{bmatrix}. \quad (5c)$$

When  $\theta = \pi$ , special cases arise for all three gates:

$$R_X(\pi) = \begin{bmatrix} 0 & -i \\ -i & 0 \end{bmatrix} = -i \begin{bmatrix} 0 & 1 \\ 1 & 0 \end{bmatrix} = -i\hat{X}, \quad (6a)$$

$$R_Y(\pi) = \begin{bmatrix} 0 & -1 \\ 1 & 0 \end{bmatrix} = -i \begin{bmatrix} 0 & -i \\ i & 0 \end{bmatrix} = -i\hat{Y}, \quad (6b)$$

$$R_Z(\pi) = \begin{bmatrix} -i & 0 \\ 0 & i \end{bmatrix} = -i \begin{bmatrix} 1 & 0 \\ 0 & -1 \end{bmatrix} = -i\hat{Z}. \quad (6c)$$

$\hat{X}$ ,  $\hat{Y}$  and  $\hat{Z}$  are called the Pauli-X, Y and Z gates respectively. The global phase  $-i$  in each Pauli gate arises because the rotation gates are derived from unitary transformations. Global phases  $e^{i\phi}$  uniformly affect all components of the quantum state and do not influence the measurement probabilities or observable outcomes. Thus, the equivalence between the Pauli gates and their respective rotation gates (up to a global phase) is valid for all practical purposes.

The Pauli-X gate plays a fundamental role in quantum computing, acting as a quantum equivalent of the classical NOT gate. It flips  $|0\rangle$  to  $|1\rangle$  and vice versa. The Pauli-Y gate combines the action of the Pauli-X gate (bit flip) with a phase flip, making it useful in certain quantum algorithms that require combined transformations, such as quantum error correction. The Pauli-Z gate is crucial for modifying the relative phase of quantum states between  $|0\rangle$  and  $|1\rangle$ , which is key to quantum interference and entanglement operations.

**2) Hadamard Gate ( $H$ ):** The Hadamard gate is a single-qubit gate that creates superposition by transforming the computational basis states  $|0\rangle$  and  $|1\rangle$  into an equal superposition of these states. It is one of the most fundamental quantum gates in quantum computing, used to initialize qubits in a superposition state.

$$H = \frac{1}{\sqrt{2}} \begin{bmatrix} 1 & 1 \\ 1 & -1 \end{bmatrix}. \quad (7)$$

$$H|0\rangle = \frac{1}{\sqrt{2}}(|0\rangle + |1\rangle). \quad (8)$$

When dealing with multiple qubits, their states and operations are represented using tensor products. For a system with  $n$  qubits, the combined quantum state is described as a vector in a  $2^n$ -dimensional Hilbert space. For example, the joint state of two qubits,  $|\psi_1\rangle$  and  $|\psi_2\rangle$ , is represented as  $|\psi_1\rangle \otimes |\psi_2\rangle = |\psi_1\psi_2\rangle$ , where  $\otimes$  denotes the tensor product. If  $|\psi_1\rangle = \alpha|0\rangle + \beta|1\rangle$  and  $|\psi_2\rangle = \gamma|0\rangle + \delta|1\rangle$ , the combined state is given by:  $|\psi_1\psi_2\rangle = (\alpha|0\rangle + \beta|1\rangle) \otimes (\gamma|0\rangle + \delta|1\rangle) = \alpha\gamma|00\rangle + \alpha\delta|01\rangle + \beta\gamma|10\rangle + \beta\delta|11\rangle$ . The probabilities of the states  $|00\rangle$ ,  $|01\rangle$ ,  $|10\rangle$ ,  $|11\rangle$  are given by  $|\alpha\gamma|^2$ ,  $|\alpha\delta|^2$ ,  $|\beta\gamma|^2$ ,  $|\beta\delta|^2$  respectively, and they sum to one.

Similarly, quantum gates applied to multi-qubit systems are represented as tensor products of individual gates. To illustrate, consider the application of a bit-flip operator or the Pauli-X gate to the first qubit of a two-qubit system initially in the state  $|00\rangle$ . The operation is represented as  $X \otimes I$ , where  $I$  is the identity gate that leaves the second qubit unchanged.

Let the initial state of the system be:

$$|00\rangle = |0\rangle \otimes |0\rangle = \begin{bmatrix} 1 \\ 0 \end{bmatrix} \otimes \begin{bmatrix} 1 \\ 0 \end{bmatrix} = \begin{bmatrix} 1 \\ 0 \\ 0 \\ 0 \end{bmatrix}. \quad (9)$$

The operator can then be represented as:

$$X \otimes I = \begin{bmatrix} 0 & 1 \\ 1 & 0 \end{bmatrix} \otimes \begin{bmatrix} 1 & 0 \\ 0 & 1 \end{bmatrix} = \begin{bmatrix} 0 & 0 & 1 & 0 \\ 0 & 0 & 0 & 1 \\ 1 & 0 & 0 & 0 \\ 0 & 1 & 0 & 0 \end{bmatrix}. \quad (10)$$

Applying  $X \otimes I$  to  $|00\rangle$ , we get:

$$\begin{bmatrix} 0 & 0 & 1 & 0 \\ 0 & 0 & 0 & 1 \\ 1 & 0 & 0 & 0 \\ 0 & 1 & 0 & 0 \end{bmatrix} \begin{bmatrix} 1 \\ 0 \\ 0 \\ 0 \end{bmatrix} = \begin{bmatrix} 0 \\ 0 \\ 1 \\ 0 \end{bmatrix} = \begin{bmatrix} 0 \\ 1 \end{bmatrix} \otimes \begin{bmatrix} 1 \\ 0 \end{bmatrix} = |1\rangle \otimes |0\rangle, \quad (11)$$

which corresponds to the state  $|10\rangle$ , showing that the  $X$  gate has flipped the first qubit while leaving the second qubit unchanged.

Like single-qubit gates, multi-qubit gates also exist in quantum computing. The Controlled-NOT ( $CNOT$ ) gate for example, is a two-qubit gate where the state of one qubit (the control qubit) determines whether the other qubit (the target qubit) is flipped. The  $CNOT$  gate is a key component in creating entangled states and forms the basis of many quantum algorithms. The  $CNOT$  gate flips the target qubit if the control qubit is  $|1\rangle$ . If the control qubit is  $|0\rangle$ , the target qubit remains unchanged. The  $CNOT$  gate is given as:

$$CNOT = \begin{bmatrix} 1 & 0 & 0 & 0 \\ 0 & 1 & 0 & 0 \\ 0 & 0 & 0 & 1 \\ 0 & 0 & 1 & 0 \end{bmatrix}. \quad (12)$$

$$CNOT|10\rangle = |11\rangle. \quad (13)$$

In addition to the  $CNOT$  gate, quantum circuits often use controlled rotation gates, which apply a rotation operation to a target qubit only when the control qubit is in the  $|1\rangle$  state. These include controlled- $R_X$ , controlled- $R_Y$  and controlled- $R_Z$  gates. In general, any unitary matrix  $U$  can be converted into a controlled- $U$  gate. Additionally, it is also possible for controlled operations to be conditioned on the control qubit being in the  $|0\rangle$  state.

Quantum gates can also be parameterized to introduce tunable parameters, providing the flexibility needed to optimize quantum circuits for specific tasks. These parameterized quantum gates form the foundation of Parameterized Quantum Circuits (PQCs), where the parameters are adjusted dynamically to perform targeted quantum transformations. A PQC operates by applying a series of parameterized unitary transformations  $U(\theta)$  to an input quantum state  $|\psi_{in}\rangle$ , yielding an output state:  $|\psi_{out}\rangle = U(\theta)|\psi_{in}\rangle$ , where  $U(\theta)$  depends on a vector of parameters  $\theta$ , which are optimized during computation.



The structure of a PQC is guided by the choice of ansatz, a circuit template designed to explore the Hilbert space efficiently. The ansatz must be expressive yet computationally feasible to enable effective optimization. Commonly used ansatzes include the hardware-efficient ansatz (Kandala et al., 2017; Leone et al., 2022; Xiao et al., 2024), which is tailored to the physical capabilities of quantum devices, and problem-inspired ansatzes (Peruzzo et al., 2014; Choquette et al., 2021; Wang et al., 2024a), which encode domain-specific knowledge.

Another critical component of quantum machine learning is the feature map, which encodes classical data into quantum states by embedding it within the quantum Hilbert space (Schuld and Killoran, 2019; Havlíček et al., 2019). This mapping process applies a sequence of quantum gates to prepare an initial quantum state that represents the input data. Two widely used encoding methods are angle embedding and amplitude embedding:

**1) Angle Embedding:** This approach encodes each classical data point  $x_i$  as the rotation angle of a quantum gate. For a classical data vector  $x = [x_1, x_2, \dots, x_n]$ , the corresponding quantum state is:

$$|\psi(x)\rangle = \otimes_{i=1}^n R_{\{X,Y,Z\}}(x_i)|0\rangle, \quad (14)$$

where  $R_{\{X,Y,Z\}}(x_i)$  represents a single-qubit rotation gate. Since quantum rotation gates are periodic,  $x_i$  must be preprocessed (e.g., scaled to  $[0, \pi]$ ) to preserve uniqueness.

**2) Amplitude Embedding:** In this method, classical data is encoded directly into the amplitudes of a quantum state. For a classical data vector:  $x = [x_1, x_2, \dots, x_N]$ , the corresponding quantum state is:

$$|\psi(x)\rangle = \frac{1}{\|x\|} \sum_{i=1}^N x_i |i\rangle, \quad (15)$$

where  $|i\rangle$  denotes the computational basis states,  $\|x\|$  ensures normalization ( $\sum |x_i|^2 = 1$ ), and  $N = 2^n$  (if  $N$  is not a power of 2, zero-padding is applied), requiring  $\log_2(N)$  qubits.

To encode floating-point data, such as a seismic trace, into the amplitudes of a quantum state  $|\psi_{seis}\rangle$ , algorithms like the Möttönen et al. (2005) state preparation method can be used to determine the architecture of the quantum embedding circuit. This algorithm constructs a quantum circuit that transforms the initial state  $|00 \dots 0\rangle$  into an arbitrary quantum state  $|\psi_{seis}\rangle$  by applying a sequence of controlled rotations. Specifically, controlled- $R_Z$  gates adjust the phases, while controlled- $R_Y$  gates adjust the amplitudes. The required rotation angles are computed based on the phases and amplitudes of  $|\psi_{seis}\rangle$ . A numerical demonstration of this algorithm is given in Example 4.1 of Chapter 4 in Schuld and Petruccione (2021).

Angle embedding is generally advantageous for smaller datasets because it relies on single-qubit rotations, making it hardware-efficient and less prone to noise. However, it does not fully exploit entanglement, which may limit its expressiveness for complex data distributions. Amplitude embedding, while more resource-intensive, offers higher data capacity by encoding data directly into the amplitudes of a quantum state. This approach is better suited for large datasets but requires deeper circuits and more controlled operations, making it challenging for near-term quantum hardware. The choice between these methods depends on dataset size, algorithmic requirements, and the available quantum hardware.

After embedding the classical dataset into the quantum Hilbert space, parameterized gates within the ansatz act on the quantum state. This process transforms the embedded state into a form that, upon measurement, provides valuable information for the learning task. The output of the quantum circuit is obtained by measuring the expectation value of a Hermitian operator  $\hat{O}$ , typically one of the Pauli operators like  $\hat{Z}$  or  $\hat{X}$ . The expectation value is given by:

$$\langle \hat{O} \rangle = \langle \psi(\theta, x) | \hat{O} | \psi(\theta, x) \rangle. \quad (16)$$

Here  $\langle \hat{O} \rangle$  represents the expected measurement outcome, and  $|\psi(\theta, x)\rangle$  is the output quantum state for a given input  $x$  and parameters  $\theta$ .

Quantum neural networks (QNNs) leverage this mechanism to perform machine learning tasks by optimizing the parameters  $\theta$  of the ansatz. This is achieved by defining a loss function  $\mathcal{L}(\theta)$  which measures the difference between the predicted and target outcomes. The expectation values of the qubits serve as the output of the quantum layer, which in case of HQNNs can be passed to subsequent classical layers (with parameters  $w$ ) for further processing. The loss function ( $\mathcal{L}(\theta)$  for QNNs and  $\mathcal{L}(\theta, w)$  for HQNNs) is then calculated and the objective is to minimize this loss, ensuring the model's parameters  $\theta$  and  $w$  are optimized for accurate predictions.

Optimization of the parameters  $\theta$  in quantum layers is typically carried out by gradient-based techniques to adjust the quantum circuit's parameters to minimize the loss function. There are multiple ways to compute this gradient:

**1) Parameter-Shift Rule:** This provides an analytical technique for calculating gradients of expectation values with respect to circuit parameters. For a parameter  $\theta$ , the gradient is determined as:

$$\frac{\partial \langle \hat{O} \rangle}{\partial \theta} = \frac{1}{2} \left[ \langle \hat{O} \left( \theta + \frac{\pi}{2} \right) \rangle - \langle \hat{O} \left( \theta - \frac{\pi}{2} \right) \rangle \right], \quad (17)$$

where  $\langle \hat{O}(\theta) \rangle$  is the expectation value of the observable  $\hat{O}$  for a given parameter  $\theta$ . This method is applicable to many quantum gates and is relatively straightforward to implement. However, it

necessitates multiple evaluations of the quantum circuit for each parameter, which can become computationally expensive, particularly for complex circuits with numerous parameters.

**2) Adjoint Method:** This is an efficient technique for computing gradients, particularly useful for simulating large quantum circuits. It calculates gradients by reversing the quantum operations in the circuit, utilizing the adjoint (conjugate transpose) of the unitary gates. The gradient of an expectation value  $\langle \hat{O} \rangle$  is computed by applying the adjoint of the unitary transformation  $U(\theta)$ , allowing for all gradients to be computed in a single backward pass instead of requiring separate evaluations for each parameter. This approach is computationally efficient, as it eliminates the need for multiple circuit runs for each parameter. However, it requires hardware or software capable of executing circuits in reverse, which is currently not feasible on most quantum hardware.

**3) Finite Difference Method:** For cases where analytical differentiation is impractical, this method serves as a numerical alternative for estimating gradients. This approach perturbs the parameter  $\theta$  by a small increment  $\delta$  and approximates the gradient as:

$$\frac{\partial \langle \hat{O} \rangle}{\partial \theta} \approx \frac{\langle \hat{O}(\theta + \delta) \rangle - \langle \hat{O}(\theta - \delta) \rangle}{2\delta}. \quad (18)$$

Although straightforward, this method can suffer from inefficiencies due to numerical approximations and the need for multiple circuit evaluations. Additionally, its performance may degrade in the presence of noise.

**4) Simultaneous Perturbation Stochastic Approximation (SPSA):** This is a gradient estimation method particularly well suited for high-dimensional quantum optimization problems. In this approach, all parameters are perturbed simultaneously in a stochastic manner, and the gradient is estimated as:

$$\frac{\partial \langle \hat{O} \rangle}{\partial \theta_i} \approx \frac{\langle \hat{O}(\vec{\theta} + \epsilon \vec{\Delta}) \rangle - \langle \hat{O}(\vec{\theta} - \epsilon \vec{\Delta}) \rangle}{2\epsilon \Delta_i}, \quad (19)$$

where  $\vec{\Delta}$  is a vector of random perturbations applied to all parameters, and  $\epsilon$  is a small scalar. SPSA is computationally efficient for optimizing large parameter spaces but may require more iterations to achieve convergence due to its stochastic nature.

Automatic differentiation further facilitates seamless propagation of gradients of the loss function with respect to both  $\theta$  and  $w$  through the hybrid quantum models, enabling efficient end-to-end optimization. The development of such frameworks necessitates robust software tools. Several open-source platforms, including Qiskit by IBM (Javadi-Abhari et al., 2024), Cirq (Google, 2020) by Google, and PennyLane (Bergholm et al., 2018) by Xanadu, provide comprehensive interfaces for designing and simulating quantum circuits, as well as integrating them with classical machine learning frameworks.

Among these, PennyLane offers a flexible framework for QML and seamlessly integrates with widely-used classical machine learning libraries such as PyTorch (Paszke et al., 2019) and TensorFlow (Abadi et al., 2016). A key feature of PennyLane is the Quantum Node, or QNode (*Figure 2*), which encapsulates a quantum circuit and enables automatic differentiation by integrating the quantum circuit with the computational graphs of classical neural networks, facilitating their gradient-based optimization within classical machine learning workflows. PennyLane also provides access to high-performance quantum simulator devices like *lightning.qubit* and *lightning.gpu*. The *lightning.qubit* device is a statevector simulator written in C++ and optimized for CPU execution, supporting the differentiation methods for efficient gradient computations in large quantum circuits. The *lightning.gpu* device is also a statevector simulator that leverages NVIDIA's cuQuantum SDK for GPU-accelerated simulations, offering significant speedups for deep and complex circuits. In this study, we utilize PennyLane in conjunction with TensorFlow to design and implement the HQ-PINN framework (*Figure 3*). We leverage its predefined templates for feature maps, ansatz circuits, simulator devices, and differentiation techniques to perform seismic inversion.

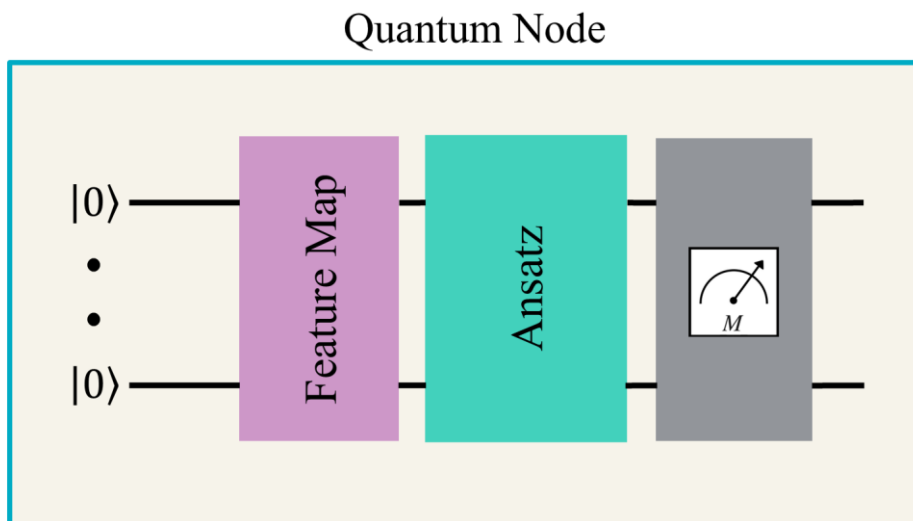


**Figure 2** A Quantum Node (QNode) comprising feature map, ansatz, and measurement operators. The feature map encodes classical data into quantum states, the ansatz employs parameterized quantum gates to process the encoded data, and the measurement operators extract meaningful classical information from the quantum states.

### Hybrid Quantum Physics-Informed Neural Networks (HQ-PINNs) for Seismic Inversion

The HQ-PINN architecture (*Figure 3*) is structured as an encoder-decoder framework that integrates hybrid quantum-classical computations to perform seismic inversion. The encoder is a HQNN that takes seismic data as an input and outputs a latent representation of the elastic parameters. The input layer is a quantum node that takes seismic data and employs the amplitude embedding feature map to leverage

quantum superposition of  $n$  qubits, enabling the encoding of data of size  $2^n$ . When the size of seismic data does not match  $2^n$ , it is padded with zeros to conform to the next nearest power of 2 before normalization for amplitude embedding. We employ the basic entangler ansatz, consisting of two layers (Figure 4). Each layer comprises parameterized single-qubit rotational gates, followed by a network of CNOT gates arranged in a closed-chain configuration. This configuration ensures that every qubit interacts with its neighbour, forming a continuous loop, making this structure well-suited for quantum neural networks. The quantum measurement yields the expectation values of the Pauli-Z operator (Figure 4), which corresponds to measurements in the computational basis. The expectation values are subsequently fed into a single classical fully connected layer, where the number of output nodes corresponds to the total dimensionality of the elastic parameters to be estimated. This layer utilizes a sigmoid activation function to scale the outputs between 0 and 1, facilitating their rescaling within the known ranges of the elastic parameters before they are passed as input to the decoder.

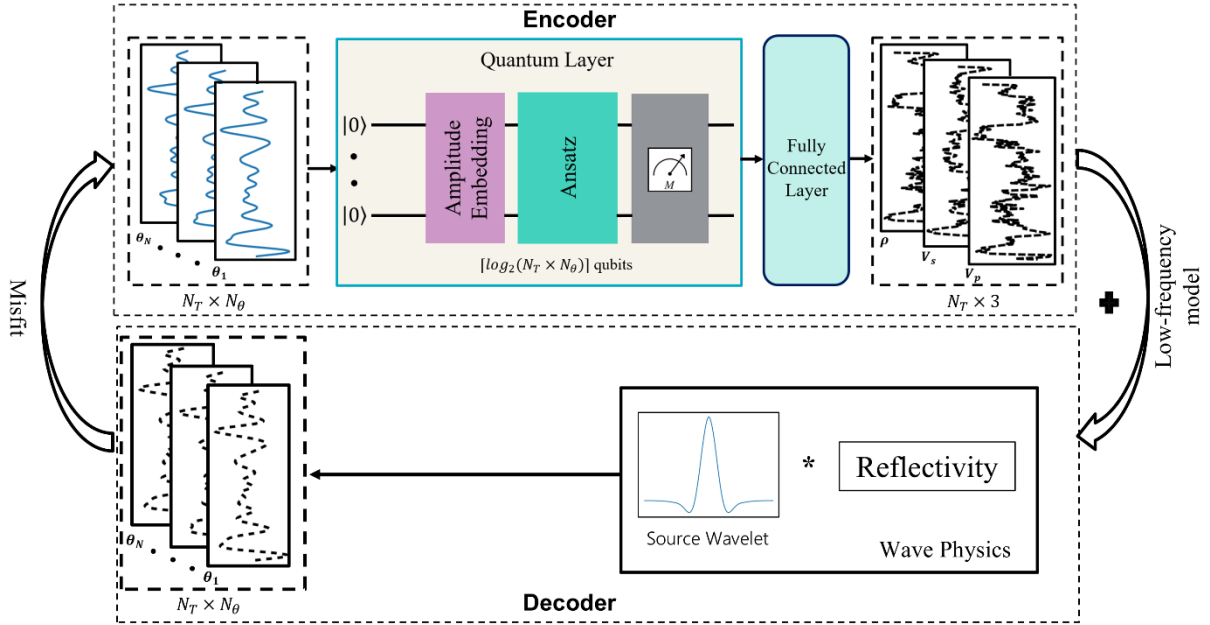


**Figure 3** The HQ-PINN framework for estimating elastic parameters from input seismic data.  $N_T$  represents the number of time samples, and  $N_\theta$  denotes the number of angle gathers. The encoder is an HQNN model that predicts the elastic parameters, which are then passed to the decoder to generate the corresponding angle gathers based on geophysical relationships. The HQ-PINN model learns by minimizing the misfit between the input and predicted seismic data from the decoder.

The decoder block utilizes the elastic parameters predicted by the encoder to generate the corresponding pre-stack and post-stack seismic data using Aki-Richards relations (Aki and Richards, 2002). For the 2D field post-stack case study, normal-incidence reflectivities are directly computed and subsequently convolved with a source wavelet to generate seismic data. This eliminates the computational burden

associated with storing large forward modeling matrices. The loss function consists of seismic misfit and a regularization term. The seismic misfit is calculated as the root mean squared error (RMSE) between the true (observed) and predicted seismic data from the decoder. The regularization term penalizes deviations of the predicted elastic parameters from a background or low-frequency trend. In seismic inversion, a low-frequency model is often incorporated (in this case, as a regularization term) to compensate for the lack of low-frequency information in the post-stack or angle-stack seismic data. This low-frequency model helps stabilize the inversion process and ensures that the solution remains physically meaningful. After computing the loss, TensorFlow’s automatic differentiation is used to update the model parameters and backpropagate the misfit through the decoder into the encoder, ensuring efficient end-to-end optimization. A key step in this process involves computing gradients within the quantum circuit. Unless otherwise specified, we employ the adjoint differentiation method to calculate exact derivatives on the *lightning.qubit* simulator. Furthermore, we use the Adam optimizer (Kingma and Ba, 2014) with a learning rate of 0.1 to update the model parameters during training.

In this study, HQ-PINN operates in an unsupervised setting, leveraging geophysical relationships to learn the underlying physics and estimate P- and S-impedances from the input seismic data. The HQ-PINN framework is highly flexible and can be readily adapted to a supervised setting when sufficient labelled data are available for training the network.

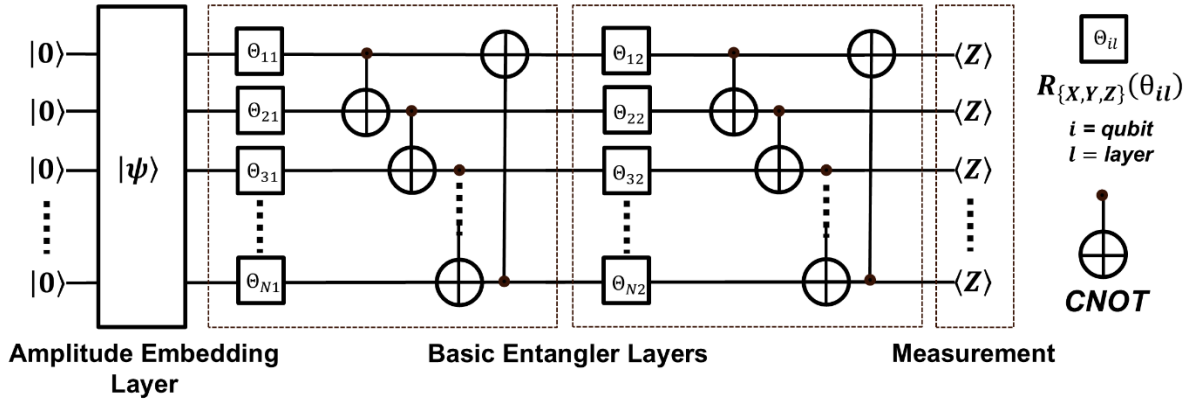


**Figure 4** The quantum node/layer utilized in the encoder of the HQ-PINN framework for N-qubits. It employs an amplitude embedding feature map and basic entangler layers ansatz, with measurements performed in the computational basis.

### Synthetic Post-stack Seismic Inversion

For the synthetic post-stack seismic case study, we employed the same dataset as Vashisth and Mukerji (2022) but focused on estimating acoustic impedances from seismic traces instead of porosities. Each seismic trace comprises 246 time samples; to facilitate amplitude embedding using 8 qubits, the traces

are padded with zero amplitudes to a length of 256. Consequently, the quantum layer is configured as an 8-qubit quantum node with an amplitude embedding feature map and a basic entangler layers ansatz. We experimented with various configurations of the basic entangler layers ansatz, incorporating  $R_X$ ,  $R_Y$  and  $R_Z$  rotation gates. Additionally, we analyzed a configuration without any ansatz, where the quantum layer includes only the feature map and no trainable parameters in the quantum circuit. In this scenario, the trainable parameters solely reside in the fully connected layer. The results, including the RMS misfit between the true and estimated acoustic impedance profiles (encoder), the true and predicted seismic traces (decoder), and the training times of the HQ-PINN model, are summarized in *Table 1*. It should be noted that the adjoint differentiation method and *lightning.qubit* simulator is used for optimizing the quantum layer. Similar results are observed across the basic entangler layer configurations utilizing  $R_X$ ,  $R_Y$  and  $R_Z$  rotation gates. The estimated acoustic impedance profile and seismic trace, from the trained HQ-PINN model incorporating the  $R_X$  rotation gate, are presented in *Figure 5* (example 1). Notably, the no-ansatz configuration also demonstrated the ability to predict accurate impedance profiles, albeit with slightly higher misfits and faster training times. These findings underscore the effectiveness of the embedding layer and its capability to encode seismic data in the quantum Hilbert space, enabling accurate seismic inversion even in the absence of an ansatz (i.e., no trainable parameters in the quantum layer), positioning the QNode as a promising candidate for an efficient dimensionality reduction tool in solving high-dimensional inversion problems.

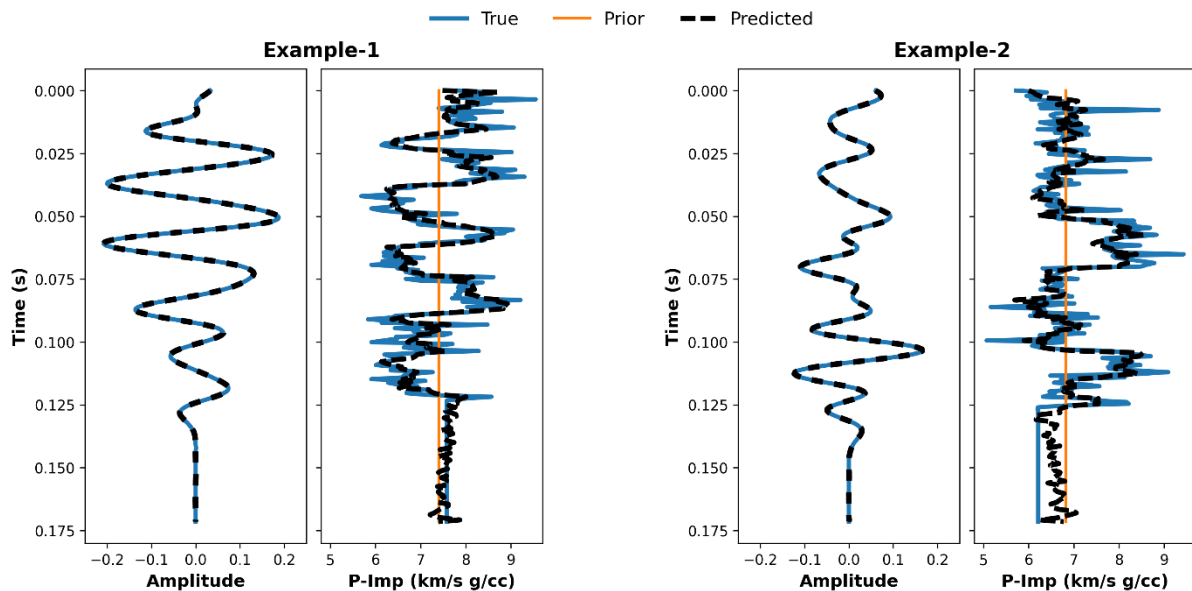


**Figure 5** HQ-PINN results for synthetic post-stack seismic examples. True seismic and acoustic impedance models are shown in blue, HQ-PINN predicted models in black, and the low-frequency prior is depicted in orange.

**Table 1** RMS misfits in the estimated seismic and acoustic impedance profiles, along with the training time for HQ-PINNs with the basic entangler layers ansatz with  $\{R_X, R_Y$  and  $R_Z\}$  rotation gates, and the case without an ansatz for post-stack inversion.

Ansatz Configuration	P-imp misfit (km/s g/cc)	Seismic misfit	Training time (s)
$R_X$	0.3712	0.000559	44.11
$R_Y$	0.3725	0.000565	45.05
$R_Z$	0.3703	0.000566	45.77
No Ansatz	0.4006	0.001107	41.36

In addition to exploring different ansatz structures, we also investigated various differentiation methods for computing gradients within the quantum node. For this experiment, we fixed the basic entangler layers ansatz with  $R_X$  rotation gates and compared the performance of four differentiation methods-adjoint, parameter-shift, finite-difference, and SPSA- in terms of accuracy and computational speed. *Table 2* lists the RMS misfit between the true and predicted acoustic impedance profiles and seismic traces, along with the corresponding HQ-PINN training times. The impedance and seismic misfits are nearly identical across all differentiation methods; however, in terms of training time, SPSA is the fastest (21.94 s), followed by the adjoint method (44.11 s), finite-difference (112.24 s), and parameter-shift (159.69 s) approaches.

SPSA is computationally the fastest, as it estimates gradients using only two function evaluations, regardless of the parameter count. However, its stochastic nature can introduce noise, potentially affecting convergence accuracy for highly complex or sensitive problems. The adjoint method offers a balance of speed and accuracy, as it computes exact gradients analytically with a cost independent of the number of parameters, making it reliable even for complex tasks. Finite-difference methods, though theoretically accurate, are slower due to requiring multiple function evaluations proportional to the number of parameters and can be prone to numerical errors caused by step-size sensitivity. Parameter-shift, while highly accurate for quantum systems due to its exact gradient computations, is the most computationally expensive, as the number of required evaluations grows with the parameter count. For complex problems, the trade-off between computational cost and accuracy becomes more significant, and selecting or adapting differentiation methods to the problem's characteristics is essential.

**Table 2** RMS misfits in the estimated seismic and acoustic impedance profiles, along with the training time for HQ-PINNs with different differentiation methods in the quantum layer for post-stack inversion.



Differentiation method	P-imp misfit (km/s g/cc)	Seismic misfit	Training time (s)
<b>Adjoint</b>	0.3712	0.000559	44.11
<b>Parameter-shift</b>	0.3712	0.000558	159.69
<b>Finite-difference</b>	0.3711	0.000556	112.24
<b>SPSA</b>	0.3781	0.000787	21.94

We applied the HQ-PINN model with a basic entangler layers ansatz utilizing  $R_x$  gates and the adjoint differentiation method to invert another post-stack seismic trace (Example 2, *Figure 5*). The predicted acoustic impedance profile and seismic trace demonstrate a close match with their true counterparts, as illustrated in *Figure 5*. The RMS misfits for the acoustic impedance and seismic data are 0.4042 km/s·g/cc and 0.000653, respectively, with the training time similar to that of Example 1.

### Synthetic Pre-stack Seismic Inversion

To further assess the efficacy of HQ-PINNs, we extend their application to the inversion of pre-stack seismic data. For this study, we utilized the P- and S- impedance dataset provided by Das and Mukerji (2020) and generated angle gathers at incident angles of  $5^\circ$ ,  $15^\circ$ , and  $25^\circ$  using a 40 Hz Ricker wavelet. We tested the HQ-PINN framework on two examples, as illustrated in *Figure 6*. For these examples, the quantum layer of the encoder is configured with a 10-qubit quantum node, utilizing an amplitude embedding feature map and a basic entangler layer ansatz with  $R_x$  gates. The HQ-PINN model is trained for 500 epochs, with the entire training process completed in approximately one minute. The RMS misfits between the true and predicted P- and S- impedance profiles, as well as the true and predicted seismic data across all angle gathers, are summarized in *Table 3*. The predicted P- and S-impedances (encoder), along with their seismic angle gathers (decoder), closely match the true data (*Figure 6*), as indicated by the low RMSE values. These results underscore the capability of HQ-PINNs to efficiently estimate impedance profiles from pre-stack seismic data.

**Table 3** RMS misfits in the HQ-PINN estimated seismic, acoustic and shear impedance profiles for pre-stack inversion examples.

Misfit	Example 1	Example 2
<b>Seismic [<math>5^\circ</math>]</b>	0.00094	0.00084
<b>Seismic [<math>15^\circ</math>]</b>	0.00103	0.00089
<b>Seismic [<math>25^\circ</math>]</b>	0.00117	0.00102
<b>P-imp (km/s g/cc)</b>	0.4567	0.4875

<b>S-imp (km/s g/cc)</b>	0.2389	0.2463
--------------------------	--------	--------

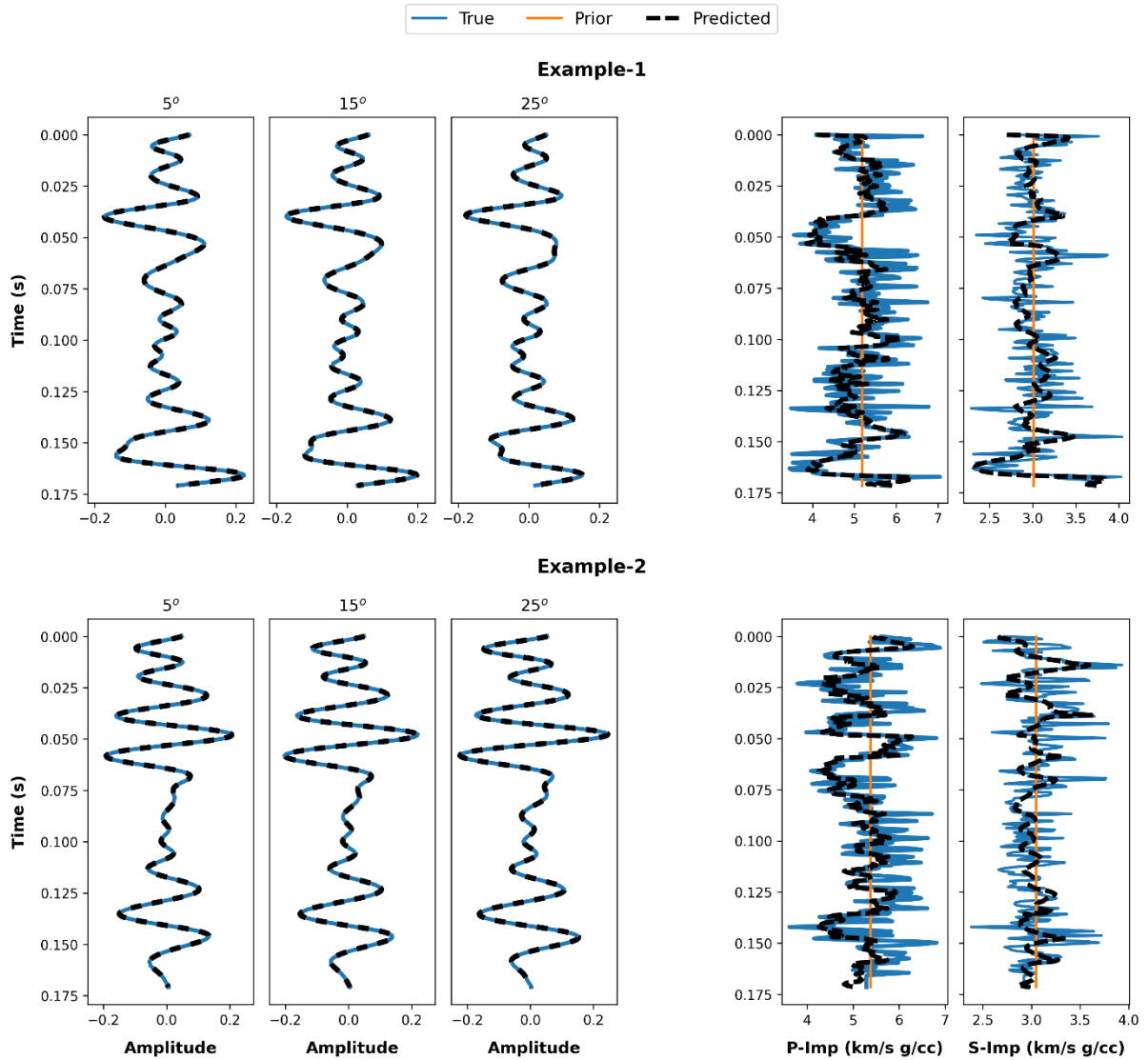


**Figure 6** HQ-PINN results for synthetic pre-stack seismic examples with angle gathers of 5°, 15°, and 25°. True seismic angle gathers, acoustic and shear impedances are shown in blue, HQ-PINN predicted models in black, and the low-frequency prior is depicted in orange.

### Performance on the Sleipner Dataset

To evaluate the real-world applicability of the HQ-PINN model, we applied it to the well-known Sleipner dataset, derived from the Sleipner CO<sub>2</sub> storage project in the North Sea- one of the world’s first large-scale CO<sub>2</sub> sequestration initiatives (Torp and Gale, 2004). This dataset includes seismic data acquired from the Utsira Sand formation, a highly porous sandstone reservoir overlain by impermeable caprock, making it ideal for CO<sub>2</sub> storage. The dataset captures the temporal evolution of CO<sub>2</sub> injection

into the reservoir, providing valuable insights into the spatial and volumetric distribution of CO<sub>2</sub> over time. Romero et al. (2023) implemented a joint inversion-segmentation approach on the Sleipner 4D post-stack seismic dataset, and we utilized the same dataset and wavelets to test the HQ-PINN framework. Specifically, we focus on 2D subsections (200 × 200) around the Utsira formation for the baseline (1994) and monitor (2001) surveys, where CO<sub>2</sub> injection had occurred.

To calibrate the HQ-PINN workflow, we first inverted the inline seismic subsection from the baseline survey passing through the well location (Baseline-1). A 16-qubit quantum node is employed, utilizing an amplitude embedding feature map and a basic entangler layers ansatz with  $R_x$  gates. The HQ-PINN model is trained for 200 epochs, and the predicted acoustic impedances (encoder output) are presented in *Figure 7* (Baseline-1). *Figure 7* also includes results obtained using least-squares inversion with Tikhonov regularization (LS-TR, Romero et al., 2023), which applies the Laplacian as a regularization operator to enforce smoothness in the predicted acoustic impedance model. The well data and the acoustic impedances derived from both the HQ-PINN model and the LS-TR method are displayed in *Figure 8*. At the well location, the estimated acoustic impedances show close alignment with the impedance log data, with RMSE of 0.576 km/s·g/cc for the HQ-PINN model and 0.595 km/s·g/cc for the LS-TR method. Furthermore, the observed and predicted seismic sections (decoder) based on the estimated acoustic impedance model (encoder) exhibit strong agreement, achieving an RMSE of 0.0783, as shown in *Figure 9*. Additionally, we inverted an inline seismic subsection near the CO<sub>2</sub> injection site from the baseline survey using the same HQ-PINN configuration. The predicted acoustic impedance model and seismic section for this case (Baseline-2) are shown in *Figures 7* and *9*, respectively. The RMSE between the true and predicted seismic sections for the Baseline-2 survey is 0.0693. The training time for both baseline surveys is approximately 100 seconds using the *lightning.qubit* simulator device.

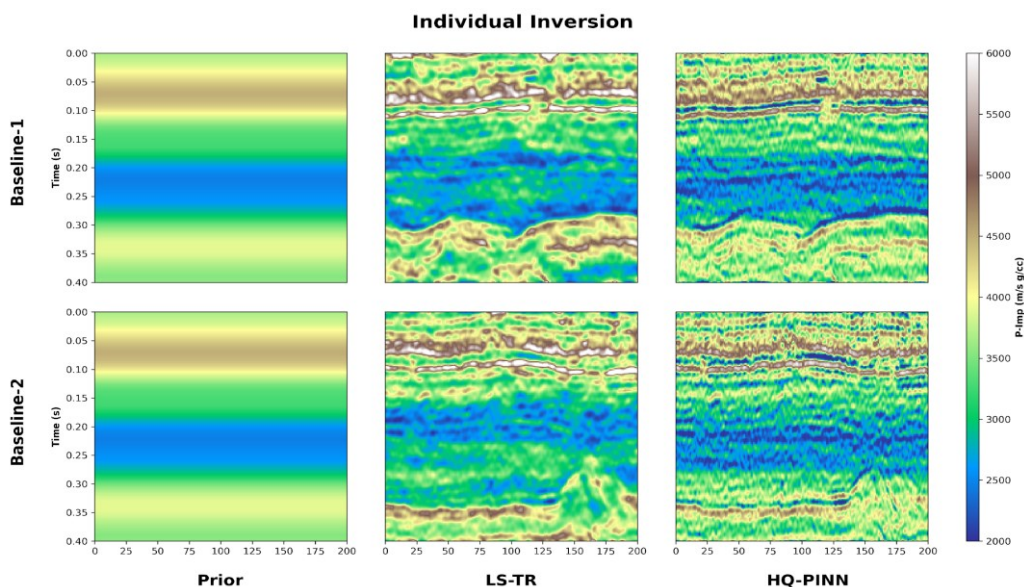


**Figure 7** HQ-PINN predicted acoustic impedance models for the individual inversion of baseline seismic surveys: Baseline-1, passing through the well location, and Baseline-2, near the CO<sub>2</sub> injection site. The results are compared with both the low-frequency prior and least-squares inversion with Tikhonov regularization (LS-TR) predictions.

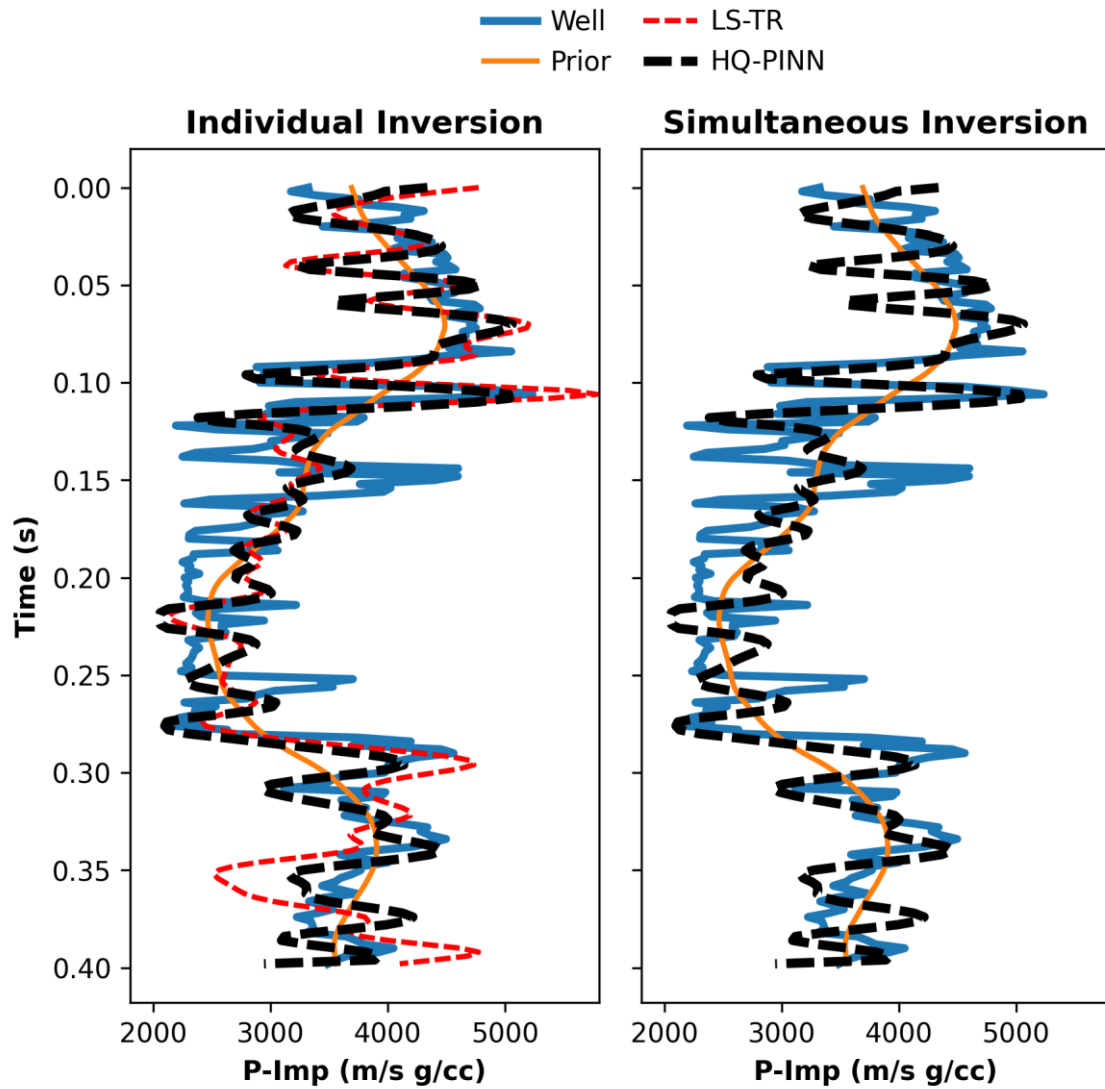


**Figure 8** HQ-PINN predicted acoustic impedances for the individual and simultaneous inversion of the Sleipner baseline seismic dataset (Baseline-1) at the well location. The predictions are compared to the impedance log, the low-frequency prior model, and the results from LS-TR inversion for the individual inversion case.

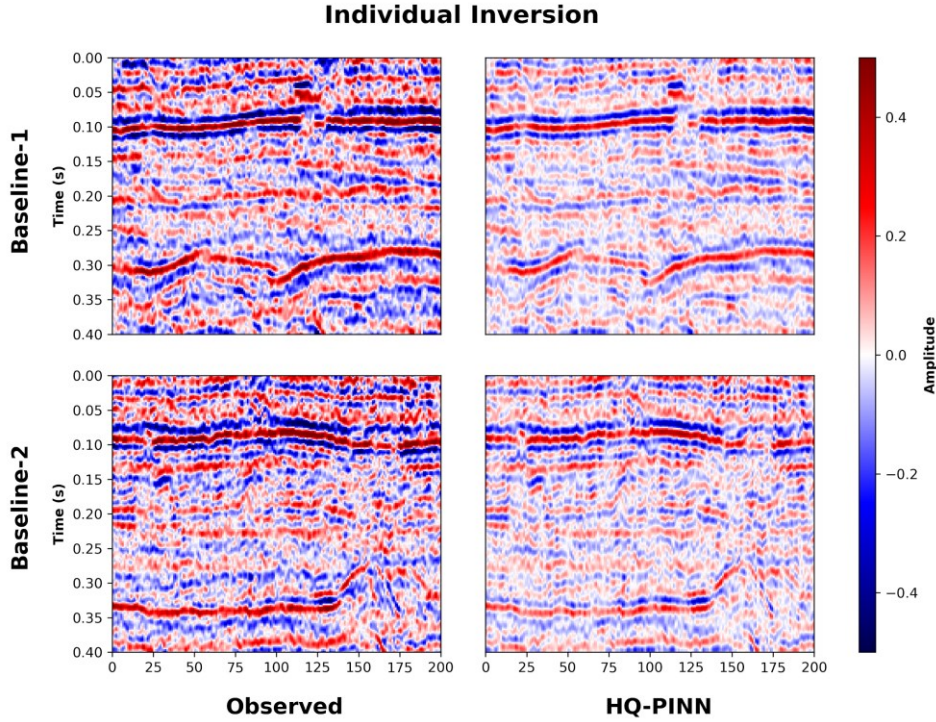


**Figure 9** Observed and predicted seismic sections from the HQ-PINN decoder for the individual inversion of baseline seismic surveys: Baseline-1, passing through the well location, and Baseline-2, near the CO<sub>2</sub> injection site.

To demonstrate the scalability and computational efficiency of integrating quantum technology into state-of-the-art classical computing workflows, we also inverted both the seismic sections (Baseline-1 and Baseline-2) simultaneously. Notably, this simultaneous inversion required only one additional qubit to encode and invert both 2D seismic sections. By increasing the number of qubits in the quantum layer from 16 to 17, we input both seismic sections into the HQ-PINN framework and estimate acoustic impedance models similar to those predicted with separate individual inversions. *Figures 10 and 11* illustrate the estimated acoustic impedance models and seismic sections for both baseline surveys using the HQ-PINN simultaneous inversion framework. *Figure 8* shows that the estimated acoustic impedances at the well location closely aligns with the individual inversion prediction and shows good agreement with the impedance log, achieving an RMSE of 0.576 km/s·g/cc.

For all previous case studies, we used the *lightning.qubit* simulator as the quantum device. This is because for quantum circuits with relatively low qubit and gate counts, the overhead associated with GPU memory transfer and kernel initialization outweighs the computational benefits of parallelization. In such scenarios, the highly optimized CPU-based implementation in *lightning.qubit* achieves faster execution times. However, for circuits involving higher qubit counts and dense gate operations, the parallelism inherent in GPU architectures significantly accelerates computations. This is evident in the Sleipner field case study, where the simultaneous inversion required 17 qubits. Utilizing the

*lightning.gpu* simulator led to a substantial reduction in training time- from 116.5 seconds to 41.77 seconds (a 64.15% decrease)- while maintaining identical accuracy in results. Furthermore, the SPSA differentiation method on the *lightning.gpu* simulator achieved similar results with an even shorter training time of 25.06 seconds. Pushing the limits further, we removed the ansatz from the quantum layer, utilizing the quantum layer solely as a dimensionality reduction tool, with learnable parameters confined to the output classical fully connected layer. Remarkably, this configuration also yielded comparable and accurate results, with training times of 35.46 seconds on the *lightning.qubit* device and 31.49 seconds on the *lightning.gpu* device, further demonstrating the efficiency and efficacy of the HQ-PINN framework. All results for the Sleipner simultaneous inversion case study are summarized in *Table 4*.

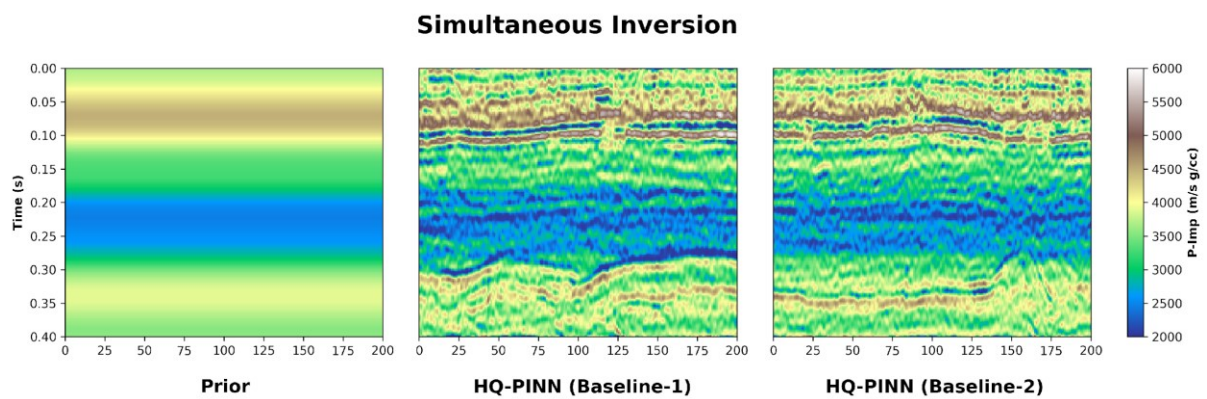


**Figure 10** HQ-PINN predicted acoustic impedance models for the simultaneous inversion of baseline seismic surveys: Baseline-1, passing through the well location, and Baseline-2, near the CO<sub>2</sub> injection site.

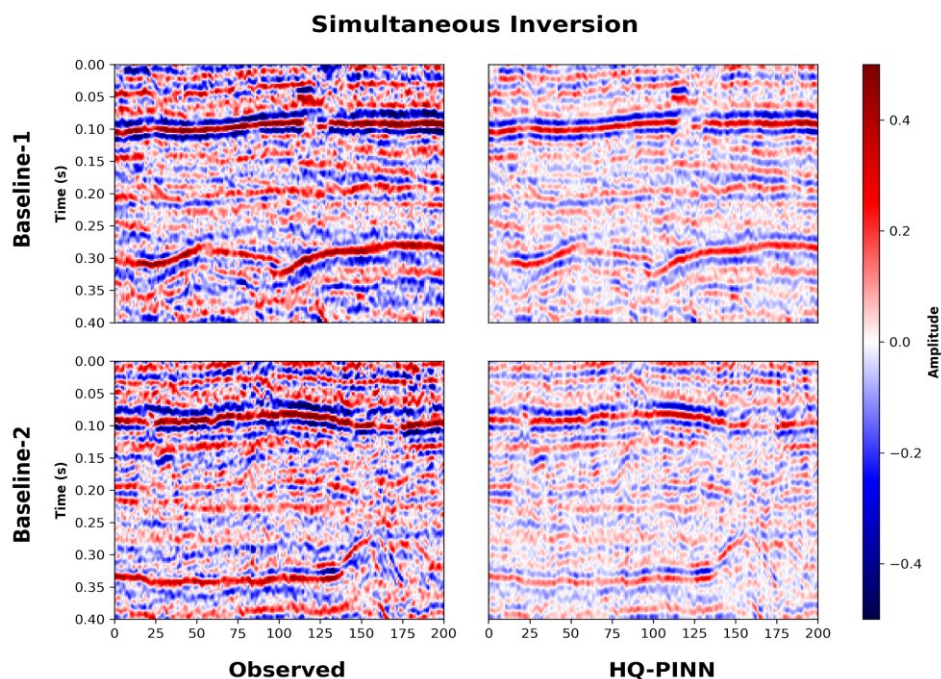


**Figure 11** Observed and predicted seismic sections from the HQ-PINN decoder for the simultaneous inversion of baseline seismic surveys: Baseline-1, passing through the well location, and Baseline-2, near the CO<sub>2</sub> injection site.

**Table 4** RMS misfits in the HQ-PINN estimated seismic sections for the simultaneous inversion of baseline seismic surveys, along with the training time across various quantum devices (simulators), ansatz configurations and differentiation methods.

Device	<i>lightning.qubit</i>	<i>lightning.gpu</i>	<i>lightning.gpu</i>	<i>lightning.qubit</i>	<i>lightning.gpu</i>
Ansatz	B.E. with $R_X$	B.E. with $R_X$	B.E. with $R_X$	No Ansatz	No Ansatz
Diff. method	Adjoint	Adjoint	SPSA	Adjoint	Adjoint
Baseline-1	0.0783	0.0783	0.0783	0.0783	0.0783
Baseline-2	0.0808	0.0808	0.0808	0.0808	0.0808
Time (s)	116.5	41.77	25.06	35.46	31.49

We further extend our analysis to CO<sub>2</sub> monitoring near the injection site. The acoustic impedance model estimated by the HQ-PINN framework for the Baseline-2 survey (1994) is smoothed and utilized as the initial/prior model for the monitor survey (2001). The resulting estimated acoustic impedance model and seismic section for the monitor survey are presented in *Figure 12*, showing an RMSE of 0.1506 between the observed and predicted seismic data. Notably, the HQ-PINN framework successfully delineates the CO<sub>2</sub> plume in both the estimated seismic section and acoustic impedance model.

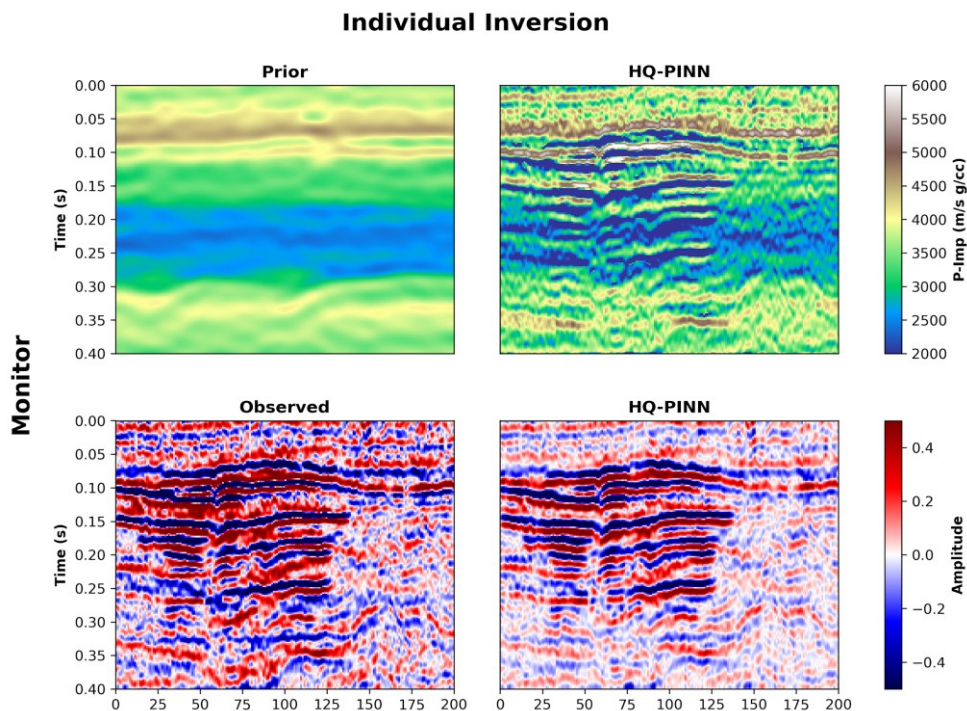


*Figure 12* HQ-PINN predicted seismic and acoustic impedance model for the individual inversion of monitor seismic survey (observed) near the CO<sub>2</sub> injection site.

## Discussion

This paper explores a novel application of QML in seismic inversion, laying the groundwork for integrating quantum computing into geophysical workflows. Specifically, we demonstrate how quantum computing frameworks can be effectively combined with classical machine learning to implement seismic inversion, estimating P- and S-impedances from post-stack and pre-stack seismic data using Hybrid Quantum Physics-Informed Neural Networks (HQ-PINNs).

In all case studies, quantum circuits were implemented using the PennyLane library, which facilitates hybrid quantum-classical computations on various quantum hardware and simulators. It is important to note that similar results can also be achieved using other quantum programming platforms, such as Qiskit and Cirq, although terminologies like feature maps, ansatz, and their pre-defined templates may differ across platforms. For this study, we utilized the amplitude embedding feature map to exploit the power of quantum superposition in encoding high-dimensional seismic data. However, alternative embedding strategies, such as angle embedding, could also be considered for their hardware efficiency, particularly for near-term quantum devices when input seismic data is not very high dimensional. Additionally, the HQ-PINN framework can be seamlessly adapted to support automatic differentiation using libraries such as JAX or PyTorch with minimal modifications.

For the synthetic case studies, the HQ-PINN model was trained for 500 epochs. Although the model trained rapidly, training was not truncated before reaching 500 epochs. The learning curves indicate that convergence was achieved, and similar results were obtained after just 250 epochs, suggesting that practical applications could further reduce training time by truncating earlier. SPSA emerged as the fastest and most efficient differentiation technique across synthetic and field case studies, delivering accurate results comparable to other differentiation methods. However, as the problem complexity increases, its stochastic nature may impact accuracy, potentially making other differentiation methods more reliable for ensuring precise gradients in intricate quantum circuits.

It is important to acknowledge that the quantum devices (simulators) employed in this study did not incorporate the effects of noise. Future work will address this limitation by utilizing noisy simulators to emulate the effects of real-world quantum hardware. This will necessitate running quantum circuits multiple times (using a large number of shots) to mitigate the effects of noise and compute reliable gradients. This step is important for preparing HQ-PINNs for deployment on actual quantum hardware. The landscape of quantum hardware is rapidly evolving, and various platforms hold unique potential



for advancing QML applications in geophysics. Superconducting qubits (e.g., IBM Quantum, Rigetti, Google Quantum AI), photonic quantum systems (e.g., Xanadu, PsiQuantum), neutral atoms (e.g., QuEra, Pasqal), and trapped ions (e.g., IonQ, Honeywell Quantum Solutions) are all promising technologies. Each hardware platform comes with its distinct advantages: superconducting qubits excel in scalability and gate fidelity, photonic systems offer room-temperature operation and speed, neutral atoms provide large-scale highly configurable qubit arrays, and trapped ions deliver long coherence times and precise control. In future work, we plan to test HQ-PINNs across these platforms to leverage their technological advancements and evaluate their suitability for geophysical applications. Furthermore, we aim to extend our proposed framework to Full Waveform Inversion (FWI), addressing the limitations of classical FWI workflows and unlocking new possibilities for high-resolution subsurface imaging.

## Conclusion

Quantum computing holds transformative potential for addressing computationally intensive problems across various scientific domains, and geophysics is no exception. By leveraging the principles of quantum mechanics, quantum computers have the potential to significantly enhance efficiency in solving high-dimensional processing and imaging problems, which are prevalent in geophysical workflows. To the best of our knowledge, this work presents the first application of QML for subsurface imaging, with a specific focus on seismic inversion to estimate P- and S-wave impedances from post-stack and pre-stack seismic data. We introduce hybrid quantum physics-informed neural networks (HQ-PINNs) and demonstrate their efficacy across synthetic and field case studies. In the HQ-PINN model, the quantum layer serves as the input layer and consists of an amplitude embedding feature map, basic entangler layers (ansatz) with  $R_X$ ,  $R_Y$  or  $R_Z$  rotation gates, and measurements in the computational basis. Notably, the choice of  $R_X$ ,  $R_Y$  or  $R_Z$  gates yielded accurate and similar results. Interestingly, even the no-ansatz configuration (i.e., no trainable parameters in the quantum layer) produced accurate predictions, underscoring the effectiveness of the embedding layer. This capability to encode seismic data in the quantum Hilbert space demonstrates the QNode’s potential as a robust dimensionality reduction tool for solving high-dimensional imaging problems. The performance of the HQ-PINN model is influenced by the quantum device and the differentiation method used to train the quantum layer. For smaller circuits, the *lightning.qubit* simulator was faster than the *lightning.gpu* device, primarily due to reduced overhead and efficient CPU-based optimizations. However, as the circuit size increased, the GPU’s ability to handle larger state spaces in parallel become evident, as seen with the *lightning.gpu* device offering significant speedups for the Sleipner simultaneous inversion case with a 17-qubit configuration. Among differentiation methods, SPSA and adjoint emerged as the most efficient, with SPSA being quicker than adjoint. SPSA achieves its speed by approximating the gradient through simultaneous perturbation of all parameters, requiring only two function evaluations per

iteration regardless of the parameter count. The adjoint method is also efficient, as it computes the gradient using a single forward pass and a backward pass, leveraging the circuit structure for scalability. Finite difference is slower because it estimates the gradient by perturbing each parameter individually, resulting in multiple function evaluations for each parameter, which becomes computationally expensive in high-dimensional parameter spaces. The parameter-shift rule requires evaluating the quantum circuit at multiple shifted parameter values per parameter, leading to significant computational overhead, but it offers analytical gradients and is compatible with quantum hardware. Thus, parameter-shift is typically slower than adjoint and SPSA but may outperform finite difference depending on implementation and hardware. In the Sleipner field case study, we performed both individual and simultaneous inversions of baseline surveys to estimate acoustic impedances. Remarkably, the simultaneous inversion required only one additional qubit to process two 2D seismic sections accurately, leveraging the power of quantum superposition. This result highlights the potential of HQ-PINNs as a highly efficient framework for addressing data-intensive geophysical problems. Even the no-ansatz configuration produced accurate results, further emphasizing the effectiveness of quantum embedding for projecting classical data into high-dimensional quantum Hilbert spaces. The HQ-PINN framework is scalable, flexible, and adaptable to various inverse problems, quantum programming frameworks, and classical automatic differentiation libraries. By demonstrating the efficacy and efficiency of HQ-PINNs across multiple case studies, this work not only underscores the potential of hybrid QML for geophysical applications but also establishes a foundation for future research in quantum-enhanced geosciences.

### **Acknowledgements**

We acknowledge the Stanford Energy Science and Engineering Department and the sponsors of the Stanford Center for Earth Resources Forecasting (SCERF) for their support in conducting this research.

### **Data and materials availability**

Data associated with this research are available and can be obtained by contacting the corresponding author.

## References

- Abadi, M., P. Barham, J. Chen, Z. Chen, A. Davis, J. Dean, M. Devin, S. Ghemawat, G. Irving, M. Isard, et al., 2016, TensorFlow: A system for large-scale machine learning: *Proceedings of the 12th USENIX Symposium on Operating Systems Design and Implementation (OSDI 16)*, 265-283.
- Aki, K., and P. G. Richards, 2002, Quantitative seismology: University Science Books.
- Alchieri, L., D. Badalotti, P. Bonardi, and S. Bianco, 2021, An introduction to quantum machine learning: From quantum logic to quantum deep learning: *Quantum Machine Intelligence*, **3** (2), 28.
- Bernstein, E., and U. Vazirani, 1993, Quantum complexity theory: *Proceedings of the 25th Annual ACM Symposium on Theory of Computing*, 11-20.
- Bergholm, V., J. Izaac, M. Schuld, C. Gogolin, S. Ahmed, V. Ajith, M. S. Alam, G. Alonso-Linaje, B. AkashNarayanan, A. Asadi, and J. M. Arrazola, 2018, PennyLane: Automatic differentiation of hybrid quantum-classical computations: *arXiv preprint*, arXiv:1811.04968
- Biswas, R., M. K. Sen, V. Das, and T. Mukerji, 2019, Prestack and poststack inversion using a physics-guided convolutional neural network: *Interpretation*, **7** (3), SE161-SE174.
- Bravo-Prieto, C., R. LaRose, M. Cerezo, Y. Subasi, L. Cincio, and P. J. Coles, 2023, Variational quantum linear solver: *Quantum*, **7**, 1188.
- Choquette, A., A. Di Paolo, P. K. Barkoutsos, D. Sénéchal, I. Tavernelli, and A. Blais, 2021, Quantum-optimal-control-inspired ansatz for variational quantum algorithms: *Physical Review Research*, **3** (2), 023092.
- Dang, Y., N. Jiang, H. Hu, Z. Ji, and W. Zhang, 2018, Image classification based on quantum K-nearest-neighbor algorithm: *Quantum Information Processing*, **17**, 239.
- Das, V., and T. Mukerji, 2020, Petrophysical properties prediction from prestack seismic data using convolutional neural networks: *Geophysics*, **85** (5), N41-N55.
- Deutsch, D., 1985, Quantum theory, the Church-Turing principle and the universal quantum computer: *Proceedings of the Royal Society of London. A*, **400**, 97-117.

Dhara, A., and M. K. Sen, 2022, Physics-guided deep autoencoder to overcome the need for a starting model in full-waveform inversion: *The Leading Edge*, **41** (6), 375-381.

Dukalski, M., D. Rovetta, S. van der Linde, M. Möller, N. Neumann, and F. Phillipson, 2023, Quantum computer-assisted global optimization in geophysics illustrated with stack-power maximization for refraction residual statics estimation: *Geophysics*, **88** (2), V75-V91.

Farhi, E., J. Goldstone, and S. Gutmann, 2014, A quantum approximate optimization algorithm: *arXiv preprint*, arXiv:1411.4028

Farhi, E., and H. Neven, 2018, Classification with quantum neural networks on near-term processors: *arXiv preprint*, arXiv:1802.06002

Feynman, R. P., 1982, Simulating physics with computers: *International Journal of Theoretical Physics*, **21**, 467-488.

Google, 2020, Cirq: <https://doi.org/10.5281/zenodo.4062499>

Guan, W., G. Perdue, A. Pesah, M. Schuld, K. Terashi, S. Vallecorsa, and J. R. Vlimant, 2021, Quantum machine learning in high-energy physics: *Machine Learning: Science and Technology*, **2** (1), 011003.

Harrow, A. W., A. Hassidim, and S. Lloyd, 2009, Quantum algorithm for linear systems of equations: *Physical Review Letters*, **103** (15), 150502.

Havlíček, V., A. D. Córcoles, K. Temme, A. W. Harrow, A. Kandala, J. M. Chow, and J. M. Gambetta, 2019, Supervised learning with quantum-enhanced feature spaces: *Nature*, **567**, 209-212.

Henderson, M., S. Shakyia, S. Pradhan, and T. Cook, 2020, Quanevolutional neural networks: Powering image recognition with quantum circuits: *Quantum Machine Intelligence*, **2**, 2.

Javadi-Abhari, A., M. Treinish, K. Krsulich, C.J. Wood, J. Lishman, J. Gacon, S. Martiel, P.D. Nation, L.S. Bishop, A.W. Cross, B.R. Johnson, and J.M. Gambetta, 2024, Quantum computing with Qiskit: *arXiv preprint*, arXiv:2405.08810

Kandala, A., A. Mezzacapo, K. Temme, M. Takita, M. Brink, J. M. Chow, and J. M. Gambetta, 2017, Hardware-efficient variational quantum eigensolver for small molecules and quantum magnets: *Nature*, **549**, 242-246.

Kerenidis, I., J. Landman, A. Luongo, and A. Prakash, 2019, q-means: A quantum algorithm for unsupervised machine learning: *Proceedings of the 33rd International Conference on Neural Information Processing Systems*, **372**, 4134-4144.

Kingma, D. P., and J. Ba, 2014, Adam: A method for stochastic optimization: *arXiv preprint*, arXiv:1412.6980

Landman, J., N. Mathur, Y. Y. Li, M. Strahm, S. Kazdaghli, A. Prakash, and I. Kerenidis, 2022, Quantum methods for neural networks and application to medical image classification: *Quantum*, **6**, 881.

Leone, L., S. F. Oliviero, L. Cincio, and M. Cerezo, 2022, On the practical usefulness of the hardware-efficient ansatz: *arXiv preprint*, arXiv:2211.01477

Liu, M., D. Vashisth, D. Grana, and T. Mukerji, 2023, Joint inversion of geophysical data for geologic carbon sequestration monitoring: A differentiable physics-informed neural network model: *Journal of Geophysical Research: Solid Earth*, **128** (3), e2022JB025372.

Lloyd, S., M. Mohseni, and P. Rebentrost, 2014, Quantum principal component analysis: *Nature Physics*, **10** (9), 631-633.

Möttönen, M., J. J. Vartiainen, V. Bergholm, and M. M. Salomaa, 2005, Transformation of quantum states using uniformly controlled rotations: *Quantum Information and Computation*, **5**, 467-473.

Neukart, F., G. Compostella, C. Seidel, D. Von Dollen, S. Yarkoni, and B. Parney, 2017, Traffic flow optimization using a quantum annealer: *Frontiers in ICT*, **4**, 29.

Nielsen, M. A., and I. L. Chuang, 2010, Quantum computation and quantum information: Cambridge University Press.

Orús, R., S. Mugel, and E. Lizaso, 2019, Quantum computing for finance: Overview and prospects: *Reviews in Physics*, **4**, 100028.

Paszke, A., S. Gross, F. Massa, A. Lerer, J. Bradbury, G. Chanan, T. Killeen, Z. Lin, N. Gimelshein, L. Antiga, A. Desmaison, et al., 2019, Pytorch: An imperative style, high-performance deep learning library: *Proceedings of the 33rd International Conference on Neural Information Processing Systems*, 721, 8026-8037.

Peruzzo, A., J. McClean, P. Shadbolt, M. H. Yung, X. Q. Zhou, P. J. Love, A. Aspuru-Guzik, and J. L. O'Brien, 2014, A variational eigenvalue solver on a photonic quantum processor: *Nature Communications*, **5**, 4213.

Perdomo-Ortiz, A., N. Dickson, M. Drew-Brook, G. Rose, and A. Aspuru-Guzik, 2012, Finding low-energy conformations of lattice protein models by quantum annealing: *Scientific Reports*, **2**, 571.

Preskill, J., 2018, Quantum computing in the NISQ era and beyond: *Quantum*, **2**, 79.

Preskill, J., 2023, Quantum computing 40 years later: *Feynman Lectures on Computation*: CRC Press.

Rebentrost, P., M. Mohseni, and S. Lloyd, 2014, Quantum support vector machine for big data classification: *Physical Review Letters*, **113**, 130503.

Romero, J., N. Luiken, and M. Ravasi, 2023, Seeing through the CO<sub>2</sub> plume: Joint inversion-segmentation of the Sleipner 4D seismic data set: *The Leading Edge*, **42** (7), 457-464.

Sajjan, M., J. Li, R. Selvarajan, S. H. Sureshbabu, S. S. Kale, R. Gupta, V. Singh, and S. Kais, 2022, Quantum machine learning for chemistry and physics: *Chemical Society Reviews*, **51**, 6475-6573.

Schade, M., C. Bösch, V. Hapla, and A. Fichtner, 2024, A quantum computing concept for 1-D elastic wave simulation with exponential speedup: *Geophysical Journal International*, **238** (1), 321-333.

Schuld, M., I. Sinayskiy, and F. Petruccione, 2015, An introduction to quantum machine learning: *Contemporary Physics*, **56** (2), 172-185.

Schuld, M., and N. Killoran, 2019, Quantum machine learning in feature Hilbert spaces: *Physical Review Letters*, **122**, 040504.

Schuld, M., and F. Petruccione, 2021, *Machine Learning with Quantum Computers*: Springer.  
<https://doi.org/10.1007/978-3-030-83098-4>

Sebastianelli, A., D. A. Zaidenberg, D. Spiller, B. Le Saux, and S. L. Ullo, 2021, On circuit-based hybrid quantum neural networks for remote sensing imagery classification: *IEEE Journal of Selected Topics in Applied Earth Observations and Remote Sensing*, **15**, 565-580.

Sebastianelli, A., M. P. Del Rosso, S. L. Ullo, and P. Gamba, 2023, On quantum hyperparameters selection in hybrid classifiers for Earth observation data: *IEEE Geoscience and Remote Sensing Letters*, 20, 1-5.

Sharma, R., D. Vashisth, K. Sarkar, and U. K. Singh, 2024, Inversion of DC resistivity data using physics-informed neural networks: *NSG 30th European Meeting of Environmental and Engineering Geophysics*, 1-5. <https://doi.org/10.3997/2214-4609.202420019>

Shor, P. W., 1994, Algorithms for quantum computation: discrete logarithms and factoring: *Proceedings of the 35th Annual Symposium on Foundations of Computer Science*, 124-134.

Simon, D. R., 1994, On the Power of Quantum Computation: *Proceedings of the 35th Annual Symposium on Foundations of Computer Science*, 116-123.

Torp, T. A., and J. Gale, 2004, Demonstrating storage of CO<sub>2</sub> in geological reservoirs: The Sleipner and SACS projects: *Energy*, 29 (9-10), 1361-1369. [https://doi.org/10.1016/s0360-5442\(04\)00153-7](https://doi.org/10.1016/s0360-5442(04)00153-7)

Vashisth, D., and R. Lessard, 2024, Seismic impedance estimation from poststack seismic data using quantum computing: *SEG Technical Program Expanded Abstracts*, 55-59. <https://doi.org/10.1190/image2024-4093838.1>

Vashisth, D., R. Lessard, and T. Mukerji, 2025, Pre-stack and post-stack seismic inversion using quantum computing: *arXiv preprint*, arXiv:2502.03808 [quant-ph].

Vashisth, D., and T. Mukerji, 2022, Direct estimation of porosity from seismic data using rock- and wave-physics-informed neural networks: *The Leading Edge*, 41 (12), 840-846.

Wang, S., P. Wang, G. Li, S. Zhao, D. Zhao, J. Wang, Y. Fang, M. Dou, Y. Gu, Y. C. Wu, and G. P. Guo, 2024a, Variational quantum eigensolver with linear depth problem-inspired ansatz for solving portfolio optimization in finance: *arXiv preprint*, arXiv:2403.04296

Wang, S., S. McArdle, and M. Berta, 2024b, Qubit-efficient randomized quantum algorithms for linear algebra: *PRX Quantum*, 5, 020324.

Wright, L., C. Mc Keever, J. T. First, R. Johnston, J. Tillay, S. Chaney, M. Rosenkranz, and M. Lubasch, 2024, Noisy intermediate-scale quantum simulation of the one-dimensional wave equation: *Physical Review Research*, 6, 043169.

Xiao, X., H. Zhao, J. Ren, W. H. Fang, and Z. Li, 2024, Physics-constrained hardware-efficient ansatz on quantum computers that is universal, systematically improvable, and size-consistent: *Journal of Chemical Theory and Computation*, **20** (5), 1912-1922.

Zaidenberg, D. A., A. Sebastianelli, D. Spiller, B. Le Saux, and S. L. Ullo, 2021, Advantages and bottlenecks of quantum machine learning for remote sensing: *IEEE International Geoscience and Remote Sensing Symposium (IGARSS)*, 5680-5683.